Lawrence Berkeley National Laboratory

Title

Impact of Pendent Ammonium Groups on Solubility and Cycling Charge Carrier Performance in Nonaqueous Redox Flow Batteries

Permalink

https://escholarship.org/uc/item/81m5k8dq

Authors

Jesse, Kate A

Abad, Sergio Diaz

Studvick, Chad

et al.

Peer reviewed

Impact of Pendent Ammonium Groups on Solubility and Cycling Charge Carrier Performance in Nonaqueous Redox Flow Batteries

Kate A. Jesse,[a] Sergio Diaz Abad,[a] Chad Studvick,[b] Gabriel A. Andrade,[a] Sandip Maurya,[a*] Brian L. Scott,[a] Rangachary Mukundan,[a,c] Ivan A. Popov,[b*] and Benjamin L. Davis[a*]

[a]MPA-11: Materials Physics Applications, Los Alamos National Laboratory, Los Alamos, NM, 87545, USA

*Email: bldavis@lanl.gov, smaurya@lanl.gov

[b]Department of Chemistry, The University of Akron, Akron, OH, 44325, USA

*Email: ipopov@uakron.edu

[c]Present Address: Energy Conversion Group, Energy Storage and Distributed Resources Division, Energy Technologies Area, Lawrence Berkeley National Laboratory, 1 Cyclotron Road, Berkeley, CA, 94720, USA

KEYWORDS

Redox flow battery; grid-scale energy storage; redox active iron complex; density functional theory

ABSTRACT

The synthesis, characterization, electrochemical performance, and theoretical modeling of two base-metal charge carrier complexes incorporating a pendent quaternary ammonium group, [Ni(bppn-Me$_3$)][BF$_4$], **3'**, and [Fe(PyTRENMe)][OTf]$_3$, **4'**, are described. Both complexes were produced in high yield and fully characterized using NMR, IR, and UV-vis spectroscopies, as well as elemental analysis and single crystal X-ray crystallography. Solubility of **3'** in acetonitrile showed 283% improvement over its neutral precursor, while the solubility of complex **4'** was

effectively unchanged. Cyclic voltammetry indicates a ~0.1 V positive shift for all waves, with some changes in reversibility depending on the wave. Bulk electrochemical cycling demonstrates both **3'** and **4'** can utilize the second more negative wave to a degree, while **4'** ceases to have a reversible positive wave. Flow cell testing **3'** and **4'** with Fc as the posolyte reveals little improvement to cycling performance of **3'** compared with its parent complex, while **4'** exhibits reductions in capacity decay when cycling either negative wave. Post cycling CVs indicate cross over is the likely source of capacity loss in complexes **3**, **3'**, and **4'**, since there is little change in the CV trace. Density functional theory calculations indicate the ammonium group lowers the HOMO energy in **3'** and **4'**, which may impart stability to cycling negative waves while making positive waves less accessible. Overall, the incorporation of a positively charged species can improve solubility, stored electron density, and capacity decay depending on the complex, features critical to high energy density redox flow battery performance.

INTRODUCTION

As wind and solar electrical generation is gradually replacing thermal forms (nuclear, coal), the foci of research has shifted to energy storage technologies.[1] There are new investments in pumped-hydro,[2-4] the largest and least expensive form of stored energy in the United States. Pump-hydro storage has specific topological requirements which limit where it can be installed and has significant up-front building costs, which has stifled their deployment.[5-7] Currently, energy storage is dominated by Li-ion batteries. Unfortunately, Li-ion batteries are unable to meet the requirements for long duration energy storage.[8] To address issues of climate change and grid-reliability, less expensive and adaptable storage technologies are required.

One possible storage technology is the redox flow battery (RFB).[9,10] Unlike traditional secondary batteries (Li-ion), where the capacity scales with electrode size, RFBs store energy in chemical species stored in tanks separate from the cell that governs energy flow in/out of the system.[10] Originally conceived in the 1970s for the NASA program, much progress has been made with RFBs using water as a solvent.[11] These aqueous RFBs, especially those featuring vanadium analytes, have recently made the news.[12] Nonaqueous RFBs (NARFBs), by contrast, have been less explored despite holding promise with a wider electrochemical windows than that of aqueous systems, which may translate into improved storage capacity. A considerable amount of work has gone into investigating carrier molecules with stable redox events at extremely high or low voltages in an effort to take advantage of this solvent window. Recent examples include derivatives of methyl viologen, fluorenone, thioester substituted cyclopropenium, and Ni bispicolinamide complexes.[13-20]

One limiting factor of many NARFBs is the reduced solubility of the charge carrier species. Since the storage capacity is directly proportional to the concentration of the least soluble complex, one may get the false impression of a system's prospects by just measuring and evaluating a

complex at saturation in one state of charge. Common methods to increase the solubility of carriers include the incorporation of polyethylene glycol (PEG) moieties as well as the introduction of asymmetry to the carrier molecule. Alternatively, incorporation of a pendent charged group on an organic carrier or ligand of a metal complex has been shown to greatly increase solubility in some cases.[21-25] Of particular concern is a charged species that gets reduced/oxidized to a neutral state, which is typically the least soluble. Systems with solubility in the hundreds of mM range are currently among the best, though higher concentrations are likely necessary for commercialization of NARFB technology.[26] Given the success of altering ferrocene and other organic analytes' solubility with a pendent charged group,[27-34] we endeavored to evaluate if the incorporation of a quaternary alkyl ammonium group would improve the solubility and cycling performance of complexes with demonstrated NARFB histories, Ni(bppn),[35] **3**, and Fe(PyTREN),[36] **4** (Scheme 1), both of which we have experimentally characterized and theoretically modeled in the past. Herein, we describe the synthesis, solubility, cycling performance, and assess the impact of the quaternary alkyl ammonium moieties on redox flow charge carriers from experimental and theoretical perspectives. While these specific complexes do not effectively utilize the full solvent window of MeCN and have low or moderate solubilities, making them impractical for commercial use in RFBs, they are effective for examining the impact of a quaternary alkyl ammonium group and determining if this approach may yield benefits to carrier performance.
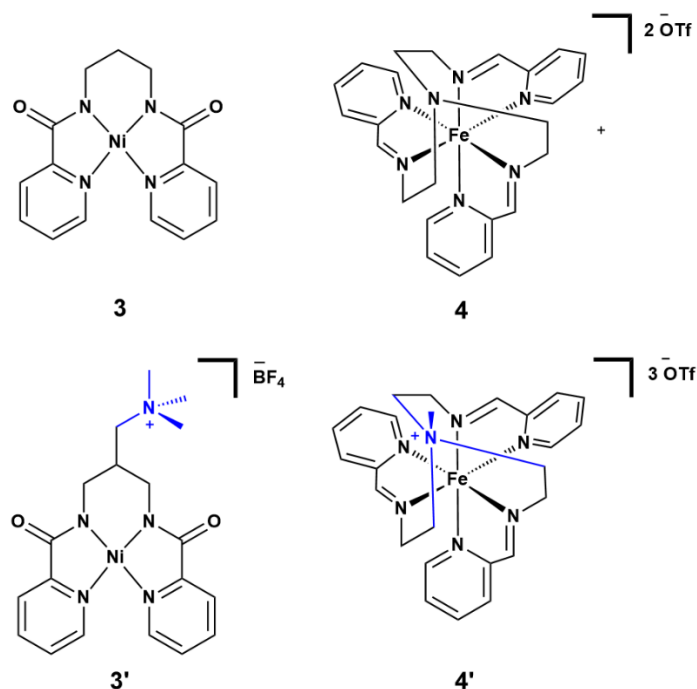
Scheme 1. Previously studied metal complexes, **3** and **4**, along with their derivatives featuring charged quaternary alkyl ammonium groups, **3'** and **4'**.

EXPERIMENTAL DETAILS

General

Standard synthetic and characterization methods were used to generate the pro-ligand **1**, followed by nickel complexation and quaternary alkyl ammonium formation to make [Ni(bppn-Me$_3$)][BF$_4$], **3'**, and anion-exchange to produce [Fe(PyTRENMe)][OTf]$_3$, **4'**. The synthesis is graphically summarized in Scheme 1. Further details and characterization data can be found in the SI. Elemental analysis (EA) was performed on **3'** and **4'** to demonstrate bulk purity.
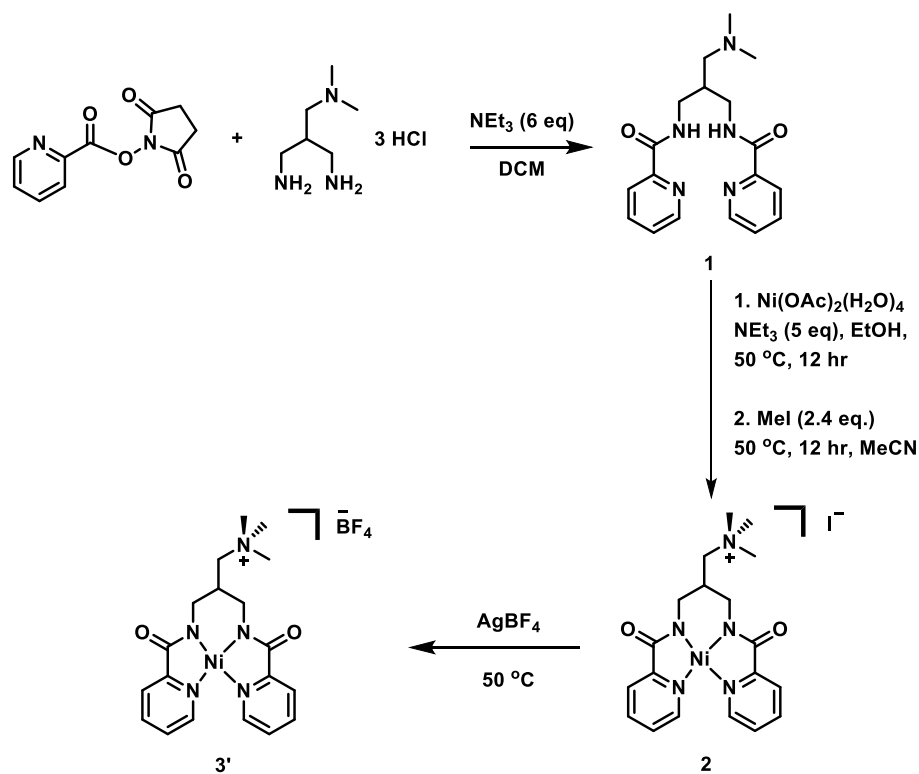
Scheme 2. Synthesis of **3'**.
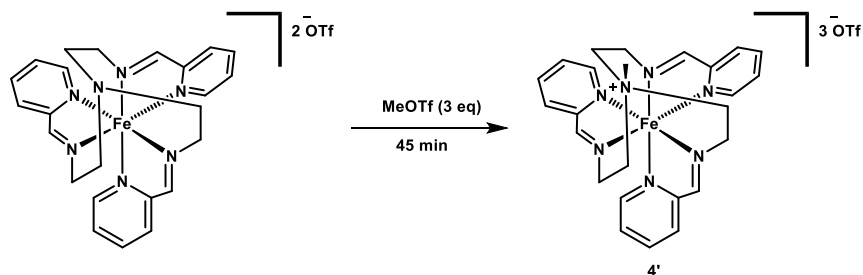
Scheme 3. Synthesis of **4'**.

Cyclic Voltammetry and Bulk Electrolysis

All electrochemical analyses including cyclic voltammetry (CV) and bulk charge/discharge experiments were performed in an Ar filled glovebox using a Metrohm PGSTAT204 potentiostat. CV was performed with a three electrode-electrochemical cell

consisting of a glassy carbon disk working electrode (0.07 cm^2, BASi), a Ag/Ag$^+$ reference electrode (BASi) containing 0.25 mM AgBF$_4$ in acetonitrile (MeCN), and a platinum wire counter electrode (23 cm, ALS). iR compensation was used after measuring the iR drop using the positive feedback tool within the Nova software, with 60-80Ω being typical with the above configuration. All scans were started 100mV more negative than the maximum potential in the sweep (indicated in Figure 2). The supporting electrolyte was tetrabutylammonium hexafluorophosphate (TBAPF$_6$, Sigma, $\geq$98%), recrystallized from absolute ethanol three times and dried under high vacuum for several hours before use. Dry MeCN and dichloromethane (DCM) were used as the solvent (purification columns from Glass contour [Laguna Beach, CA)]) and verified with Karl Fisher titration to be < 5 ppm H$_2$O (Mettler-Toledo C20, using NIST traceable standards). All CV experiments were run at 100 mV/s in MeCN electrolyte containing 1mM analyte and 0.1 M [TBA][PF$_6$] unless otherwise noted. Charge/discharge measurements were carried out with a glass H-cell with a porous glass frit (P5, Adams and Chittenden) separator. The volumes in the chambers were 10mL, with 1mM analyte concentrations. Fresh RVC was used as the working and counter electrodes and ± 1mA of current was applied during the charge and discharge cycles.

Flow Cell Testing

Flow cell testing was carried out using a symmetric electrolyte system to prevent species crossover using 40 mL of 5 mM **3'** (or **4'**) and 10 mM ferrocene in 0.25 M TEABF$_4$ solution in MeCN as posolyte and negolyte. Charge/discharge cycling was performed using a BT-G-25 battery testing station (Arbin Intruments, USA) on 10 cm^2 flow cell hardware equipped with graphite felt electrodes (2.5 mm thick, SGL Group, Germany) and a porous Celgard® separator (4560, x2 pieces) with an electrolyte flowrate of 20 mL min^{-1}. The cycling protocol consists of 50 cycles close to ~50% and ~100% of state-of-charge (SOC), as defined by voltage ranges (Table

S5). Given the variability of SOC based on voltage, due to ohmic resistance, 50 and 100% are approximate. The lack of a charge cut-off was a conscious decision to avoid accessing other waves. No positive potential ranges are provided since those waves would not cycle.

The Coulombic efficiency (CE), voltage efficiency (VE) and energy efficiency (EE) were calculated using the equations listed below:

$$CE = \frac{\int I_{discharge} \, \mathrm{dt}}{\int I_{charge} \, \mathrm{dt}} \times 100\%$$

$$EE = \frac{\int \left(V_{discharge} \times I_{discharge} \right) \mathrm{dt}}{\int \left(V_{charge} \times I_{charge} \right) \mathrm{dt}} \times 100\%$$

$$VE = \frac{EE}{CE} \times 100\%$$

where I is current, V is voltage and t are time during the charge-discharge cycling.

RESULTS AND DISCUSSION

In this study, we have examined the synthetic modification of known NARFB charge carriers with a pendent quaternary alkyl ammonium to study the impact on solubility and cyclability. Quaternary alkyl ammonium groups can be substantially smaller in size than neutral functionalities, which can have a decided impact on solubility improvements (*vide infra*). For example, polyethylene glycol (PEG) chains are often used to increase solubility of both organic and inorganic carriers.[21,22,37-42] Each ethylene glycol monomer results in an increase of 45.06 g/mol to the mass of the overall structure. However, the addition of a single ethylene glycol moiety may not substantially increase solubility, resulting in the addition of multiple repeating -CH_2CH_2O- units. As such, a significant amount of mass may be added to a carrier when the PEG functionality is used as a solubilizer. In contrast, the addition of -NMe_3^+ results in a single increase

of 59.11 g/mol to the overall molecular weight of the carrier. However, both strategies result in an overall increase in molecular weight of the complex in question.

Selection of Complexes

Two previously investigated charge carrier complexes were chosen to explore the effect of incorporating quaternary alkyl ammonium moieties into metal-ligand complexes on the solubility and cyclability of NARFB analytes. The first complex features an overall neutral Ni(II) complex with the propyl backbone linking two picolinamide ligands (**3**), while the second complex chosen was an Fe(II) complex featuring a hexadentate pyridineimine ligand and two outer sphere triflate counterions (**4**). Charged groups were incorporated in the form of quaternary ammonium cations due to the demonstrated electrochemical stability of alkyl ammonium groups to make **3'** and **4'**.[43–46] In both cases, the quaternary ammonium was attached to the ligand in such a fashion to minimize the steps required for incorporation.

Synthesis of 3' and 4'

Complexes **3'** and **4'** were made in high yield (63% and 93%, respectively) by a single (Fe) and two (Ni) step process from readily available starting materials (Schemes 1 and 2). Quaternization of the backbone N was accomplished in both cases by adding excess methylating agent to a solution of the Fe or Ni complex in MeCN and allowing the mixture to stir at room temperature. The resulting Ni complex (**3'**) was isolated and an anion exchange was performed to remove I$^-$ and incorporate the redox-silent BF$_4^-$ counterion. Single crystals were grown from a layer diffusion of Et$_2$O into a concentrated solution of **3'** in MeCN and analyzed by single crystal X-ray diffraction (SXRD). The solid state crystal structure of **3'** shows a pseudo square planar Ni(II) complex featuring a quaternary amine cation off of the ligand backbone (Figure 1). This complex features the expected low spin configuration for a square planar Ni(II) complex, as

evidenced by sharp peaks in the ^{1}H nuclear magnetic resonance (NMR) spectrum (Figure S5). Infra-red (IR) spectroscopy clearly confirms the presence of ligand C=O bonds observed in the crystal structure at 1622 and 1602 cm^{-1}. These absorbances are shifted to lower energy from the C=O bonds in the pro-ligand by 87 and 58 cm^{-1} respectively, indicating reduced double bond character by increased back-bonding (Figure S14). The neutral parent compound exhibited 1586 cm^{-1} for this same C=O, showing that the pendent quaternary ammonium group inductively removes back-bonding electron density.[35] Additionally, the N-H stretches seen in the IR spectrum of the pro-ligand disappear upon metalation, further confirming the proposed structure of **3'**.

Complex **4'** was synthesized using MeOTf as the methylating reagent rather than MeI. Not only was MeI not strong enough to methylate the N, but the use of MeOTf allowed for consistency in counterions between the previously studied **4** and the newly synthesized **4'**. Single crystals suitable for SXRD were grown via diffusion of Et$_2$O into a concentrated solution of **4'** in MeCN. The solid state structure showed the expected pseudo octahedral Fe complex featuring a hexadentate pyridineimine ligand with a methylated N on the tris(2-aminoethyl)amine (TREN) backbone and three outer sphere triflate counterions (Scheme 3, Figure 1). The ^{1}H NMR featured all diamagnetic peaks in alignment with a low spin Fe(II) center (Figure S9).
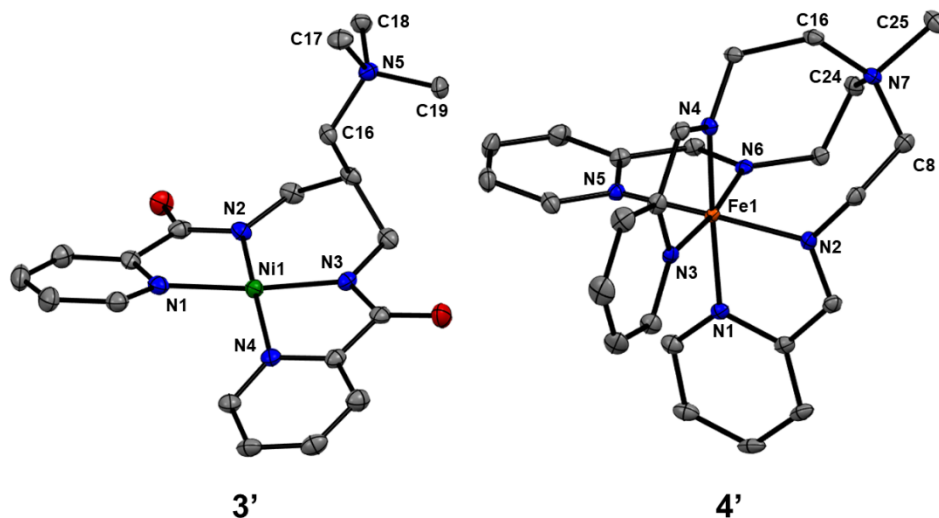
Figure 1. SXRD of **3'** and **4'**. Fe (orange), N (blue), C (gray), O (red), Ni (green). Counterions and hydrogens have been removed for clarity. Selected bond lengths for **3'** (Å), Ni1-N1: 1.931(2), Ni1-N2: 1.866(2), Ni1-N3: 1.873(2), Ni1-N4: 1.940(2), N5-C16: 1.518(3), N5-C17: 1.497(3), N5-C18: 1.506(3), N5-C19: 1.496(3). Selected bond lengths for **4'** (Å), Fe1-N1: 1.979(2), Fe1-N2: 1.935(2), Fe1-N3: 1.969(2), Fe1-N4: 1.940(2), Fe1-N5: 1.985(2), Fe1-N6: 1.931(2), N7-C8: 1.532(3), N7-C16: 1.539(3), N7-C24: 1.530(3), N7-C25: 1.529(3).

Solubility of 3' and 4'

Using UV-vis spectroscopy, we evaluated the solubility of **3'** and **4'** at room temperature (see SI for details), yielding 25.6(2) mM (0.1 M solution of [TBA][PF$_6$]/MeCN) and 0.31(2) M (in MeCN), respectively. For reference **4** had a reasonably high starting solubility of 0.54(1) M in MeCN as compared to **3** which had a solubility of 9.13(2) mM in a 0.1 M solution of [TBA][PF$_6$] in MeCN.[47,48] We realize the above evaluations were performed in different circumstances and the literature indicates a notable impact of the supporting electrolyte on carrier saturation level[49] – based on our prior experience, we estimate that solubility of **4** in equivalent supporting electrolyte would likely be half of what has been measured, e.g. ~0.25M. As such, the addition of an alkyl ammonium moiety that transforms the Ni complex into a salt has a substantial effect (283% improvement) on solubility, although the solubility of **3'** on the absolute scale is still low to be used in a commercial application. Conversely, the incorporation of an alkyl ammonium moiety

into **4** results in a small reduction in solubility, where **4'** has a maximum solubility ~0.2M lower than complex **4**. At this point we do not have a clear explanation for the reduction in solubility. There isn't an apparent correlation between functional group identity, complex molecular weight, etc. and observed solubility in other modified RFB charge carriers.[32,50,51] Attempts to isolate other charge states and evaluate their solubility to gauge any trends was stymied by poor solubility or stability of the chemical redox agents. Complex **4'** was only soluble in MeCN, precluding the use of KC$_8$, decamethylcobaltocene, or sodium naphthalenide, all of which are chemically unstable in MeCN. Stoichiometric reductions were attempted in THF despite the insolubility of **4'**, but no reaction was observed. No attempt was made to isolate the oxidized version of **4'** since that redox event proved to be irreversible and unstable to cycling (*vide infra*). Similarly, the various redox states of **3'** were not chemically isolated after determining that **4'** seemed most promising for flow cell applications and testing.
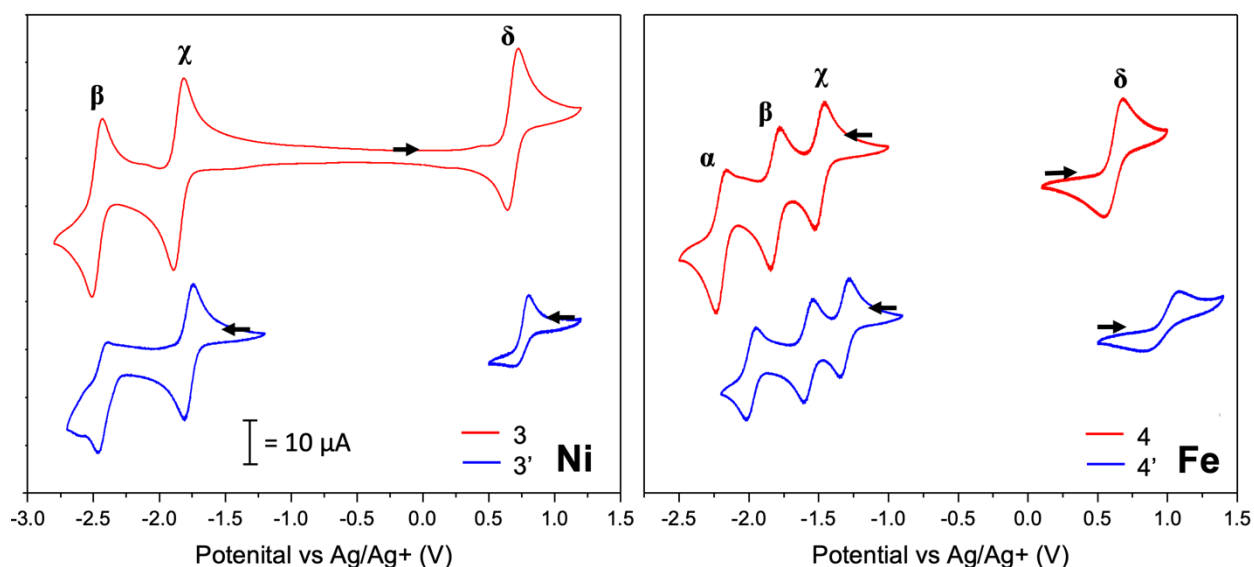
Cyclic Voltammetry

Figure 2. CV of **3** (left, red) and **3'** (left, blue), and CV of **4** (right, red) and **4'** (right, blue). **3'**, **4**, and **4'** were all run at 1 mM analyte concentration. **3** was run at 1.5 mM analyte concentration, then the current was normalized for comparison to the other complexes. All CV were run at 100

12

mV/s in 0.1 M [TBA][PF$_6$] in MeCN. For exact potentials of all redox events see Table 1. Arrows indicate the start position and direction of the sweep; plots are with the IUPAC convention.

All complexes were evaluated by CV in 0.1 M [TBA][PF$_6$] in dry MeCN (Figure 2). All complexes have the expected ligand- and metal-based redox events, as hypothesized from previous investigations.[35,36] The introduction of the quaternary ammonium to the ligand results in a positive shift for all redox events, as predicted by theory (*vide infra*). This positive shift is minimal for all ligand-based reductions, ranging from ~150 mV to ~200 mV. It is similarly minimal for the δ wave in **3'**, which exhibits a positive shift of 130 mV. However, the δ wave in **4'** is shifted positively by 350 mV as compared to the parent complex, **4**. This dramatic shift is accompanied by loss in the reversibility of this redox event as evidenced by the decrease in the peak ratio of **4'** (Table 1). Consequently, the addition of a positively charged alkyl ammonium to the ligand appears to stabilize the β wave, whose current ratio is closer to unity, compared with the β wave in **4.**

Table 1. Summary of CV data. Potentials (V) are referenced to Ag/Ag$^+$. Current ratios, *i*(cathodic)/*i*(anodic), are shown in parentheses.

E$_{1/2}$ → Complex ↓	α	β	χ	δ
3	-	−2.63 (1.05)	−2.01 (1.02)	0.53 (0.86)
3'	-	−2.51 (0.59)	−1.85 (1.03)	0.66 (1.46)
4	−2.29 (0.69)	−1.90 (0.82)	−1.58 (1.09)	0.52 (0.94)
4'	−2.07 (0.79)	−1.66 (1.03)	−1.40 (0.97)	0.87 (0.84)

Bulk electrolysis

Bulk electrolysis experiments were conducted on both **3'** and **4'** using a symmetric H-cell. When **3'** was cycled through the χ wave over 25 cycles, Coulombic efficiencies were near 100% and a utilization (n, electrons/molecule) of ~0.7 electrons for both the charge and discharge cycles was observed (Figure 3). This behavior is very similar to **3**.[35] Cycling through both the **χ and β** waves initially showed a utilization value ~2 electrons, something we had hoped to observe but rarely do for possible 2 electron carriers. This utilization value progressively decayed from a discharge value of 1.4 to 0.8 electrons over 25 cycles, similar to cycling behavior of the $Zn(L5)_2$ complex described by Sanford, indicating the special stability observed in the latter's work with nickel did not apply to our complex.[52] For the positive wave (**δ**), the irreversibility was unchanged from **3** (Figure S21).
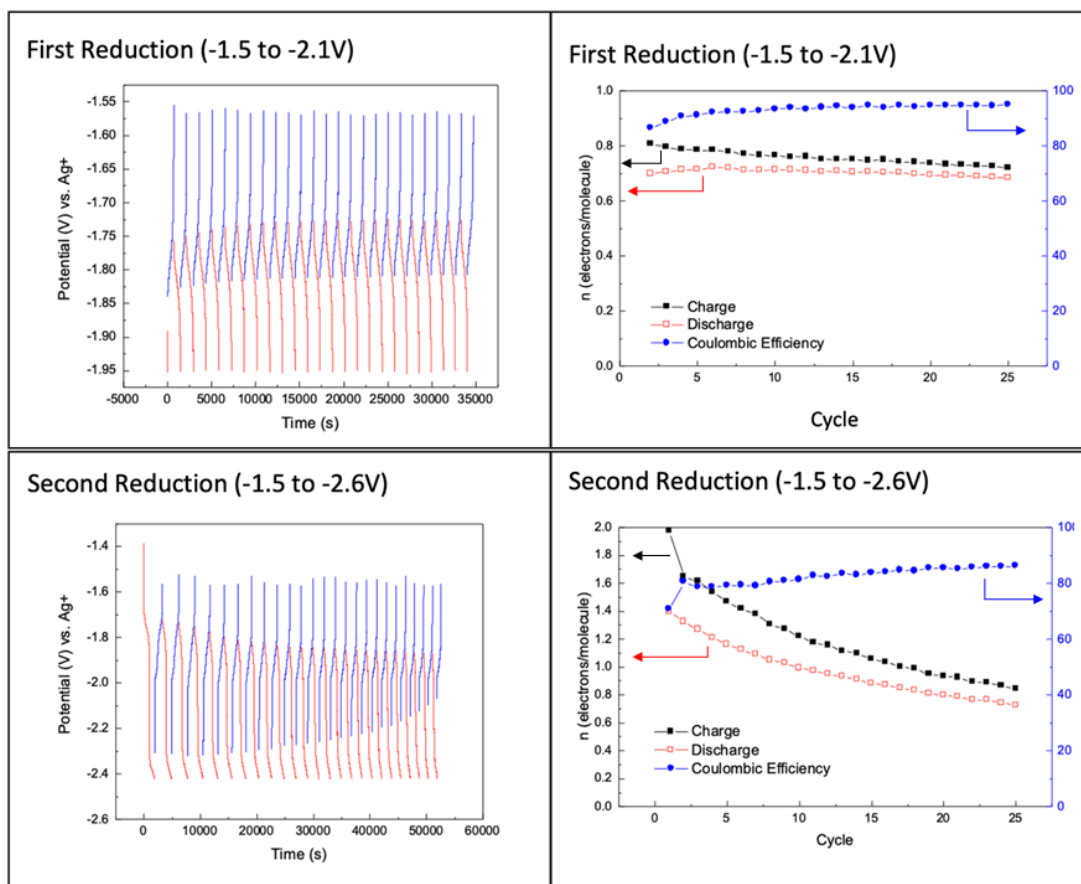
Figure 3. Bulk electrolysis data for cycling **3'**. Potential *vs.* time (top left) and utilization *vs.* cycle (top right) for the χ wave. Potential *vs.* time (bottom left) and utilization *vs.* cycle (bottom right) for χ and β waves.

Bulk cycling of the χ wave for **4'** was stable over 25 cycles (Figure 4). Utilization, however, was approximately half the magnitude compared to the parent complex. As such, the stability of **4'** compared to **4** is quite similar, but the amount of charge passed is substantially lower.[36] When cycling the χ and β waves, **4'** continues to share similar performance to **4**, except the initial utilization is lower (~1 *vs.* ~1.8 electrons/molecule as seen in the SI of ref 36).
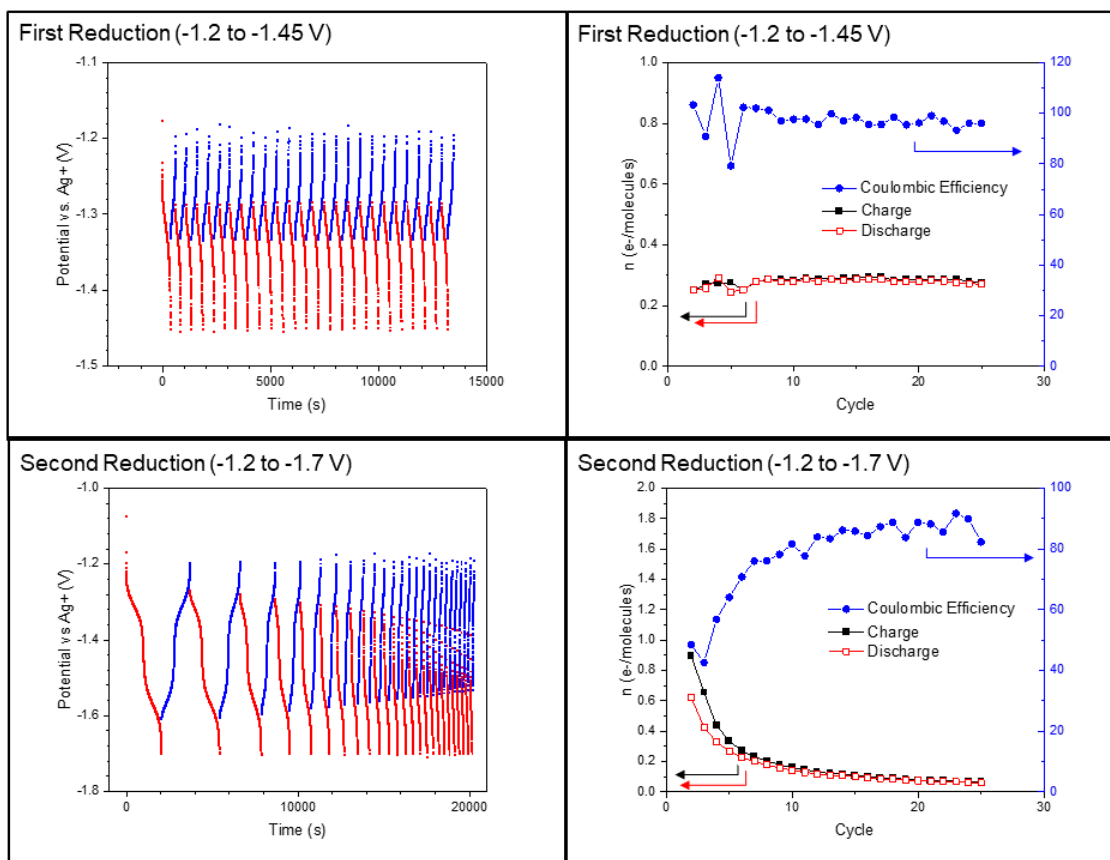
Figure 4. Bulk electrolysis data for cycling **4'**. Potential *vs.* time (top left) and utilization *vs.* cycle (top right) for the χ wave. Potential *vs.* time (bottom left) and utilization *vs.* cycle (bottom right) for χ and β waves.

Cyclability of the δ wave in **3'** and **4'**, respectively, was short lived. In contrast, the oxidative redox couple for **4** could be cycled.[35,36] This suggests that, while the inclusion of a charged cation in the ligand scaffold is beneficial for cycling multiple reductive events in first row transition metal carriers, the same pendent charged cation may be detrimental to the durability of the carrier when cycling oxidatively.

Flow Cell Cycling

Cycling of **3'** and **4'** was performed using a similar configuration as previously reported with a key change in cell surface area (10 cm^2) and the use of ferrocene as the posolyte.[36] Ferrocene

was used since neither positive wave in **3'** and **4'** cycled in bulk electrolytic experiments. Complexes were examined by first cycling thru 50% SOC of their least negative wave (χ wave), followed by ~100% SOC, and then the 2nd negative wave was accessed at 50% of its SOC (β wave). Based on the reversible nature of the χ wave in the CV and bulk electrolytic experiments for complexes **3'** and **4'**, we predicted both of these complexes would perform well in flow experiments. The easiest test, cycling through 50% SOC, indicated both **3'** (Figure S23) and **4'** (Figure S25) exhibit high Coulombic efficiencies (~95%), and modest voltage efficiencies (~85-88%). Complex **3'** is notable for showing no loss of discharge capacity, whilst complex **4'** has ~0.3%/cycle. Complex **4** also has a capacity loss of ~0.3%/cycle (Figure S24), indicating there is no benefit for a pendant ammonium at this point.

The more difficult test is cycling charge carrier complexes to ~100% SOC with their χ wave. Both complexes **3'** and **4'** cycle very well and outperform their parent complexes (Figure 5). Complex **3'** maintains the high Coulombic and voltage efficiencies with essentially no loss in discharge capacity. Complex **4'**, by contrast, does show a loss of 11.64% over 50 cycles or 0.23%/cycle – an improvement over the uncharged complex **4** under the same conditions (Figure 5, plot c). Post cycling CVs (Figure S27-30) are consistent with these performance metrics, with complex 3/3' showing virtually no change while complex 4 shows the greatest reduction in wave intensity especially on the negolytic half-cell. We would like to note that the Coulombic efficiency is curiously > 100% in complex **4'** and **4** (Figure S24, plot c)**,** resulting in the unusual situation of higher energy efficiency than voltage efficiency (Figure 5, plot b). This observed feature, which was not previously seen in control experiments (Fc, V(acac)$_3$), suggests the possibility of side reactions involving **4** and **4'** with other components in the flow cell, including Fc, especially at higher SOC levels. As a result, further experiments are being planned to gain a better understanding of this behavior.
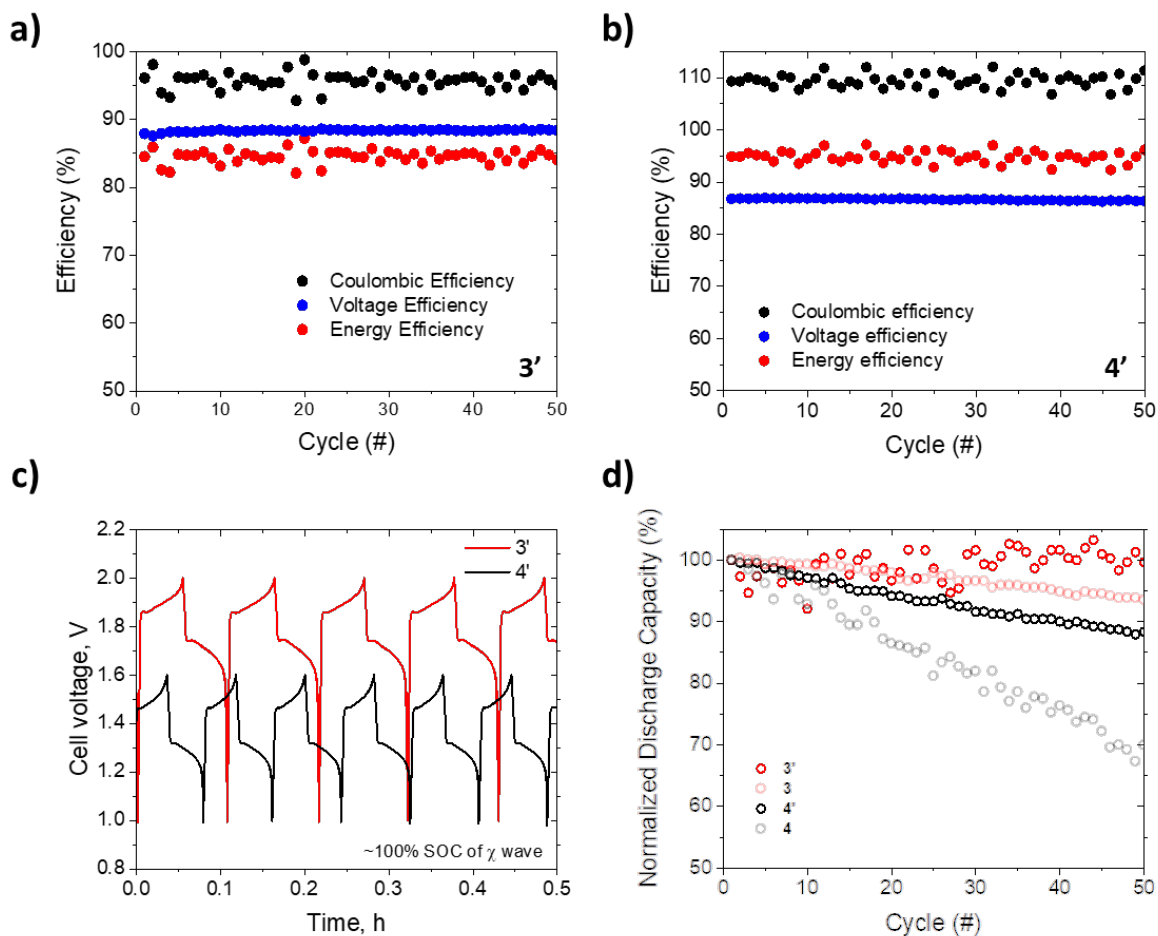
Figure 5. Charge-discharge efficiencies and cycling curves of **3'** and **4'** (plot a, b, and c) at 5 mA cm^{-2}, ~100% SOC of χ waves. Capacity retention during the charge-discharge cycles (plot d). Conditions: 5 mM **3'** and **4'**, 10 mM of Fc and 0.25 M of TEABF$_4$ in MeCN.

The more attractive quality of metal complexes like **3'/4'** is the possible use of multiple redox events per molecule, increasing the discharge capacity of the system at a fixed solubility level. The bulk cycling of **3'** indicated > 1 electron/molecule in the bulk cycling (Figure 3) suggesting that the β wave may exhibit reversibility and hence additional discharge capacity in flow experiments. Complex **4'** qualitatively showed that the χ and β waves could be accessed initially, although total utilization was not >1 (Figure 4, lower left). When complexes **3'** and **4'** were cycled in flow experiments to 50% SOC into the β wave (including the χ **wave**), we only observed a brief discharge at a higher potential in complex **3'** (Figure 6c) – in contrast to complex

18

3 (Figure S23) and **4'** (Figure 6c), which show no indication of a 2nd discharge plateau. While no distinct discharge voltage plateau was observed for **4'**, the normalized discharge capacity showed ~ 70% increase (from 4.4 Ah·mol^{-1}L^{-1} during 100% SOC cycling of χ wave to 7.4 Ah·mol^{-1}L^{-1} during 50% SOC cycling of β wave). This suggests the possibility of accessing the β wave without any noticeable voltage plateau (Figure 6, plot c and Figure S27). Similarly, **3'** exhibited a higher normalized discharge capacity of 15.8 Ah·mol^{-1}L^{-1} during 50% SOC cycling of β wave compared to 8.7 Ah·mol^{-1}L^{-1} during 100% SOC cycling of χ wave (Figure S27). These discharge capacities align well with the bulk electrolytic experiments, where the utilization of electrons determines the achievable discharge capacity. Both complexes exhibited similar initial efficiency metrics (CE ~90%, VE ~80-85%, and EE = 74-78%). After 50 cycles, complex **3'** exhibits a 37% capacity loss, which is slightly worse than the parent complex **3** with 31%. Complex **4'** performs better with 55% loss, compared to the 68% loss in complex **4**, Only complex **4** shows significant degradation in the post-cycling CV (Figure S28, bottom), largely on the negolytic portion. The contrasting stability in complex **4** and **4'** can be rationalized by the improved charge balance with a proximal positively charged NR$_3^+$ moiety in **4'**. The lack of large change in the CV of complexes **3**, **3'**, and **4'** suggests cross-over was the primary source of performance degradation and re-mixing the electrolytic solutions should restore capacity. Taken together, these results indicate incorporating a charged pendant ammonium can improve cycling of specific waves within certain metal complexes.
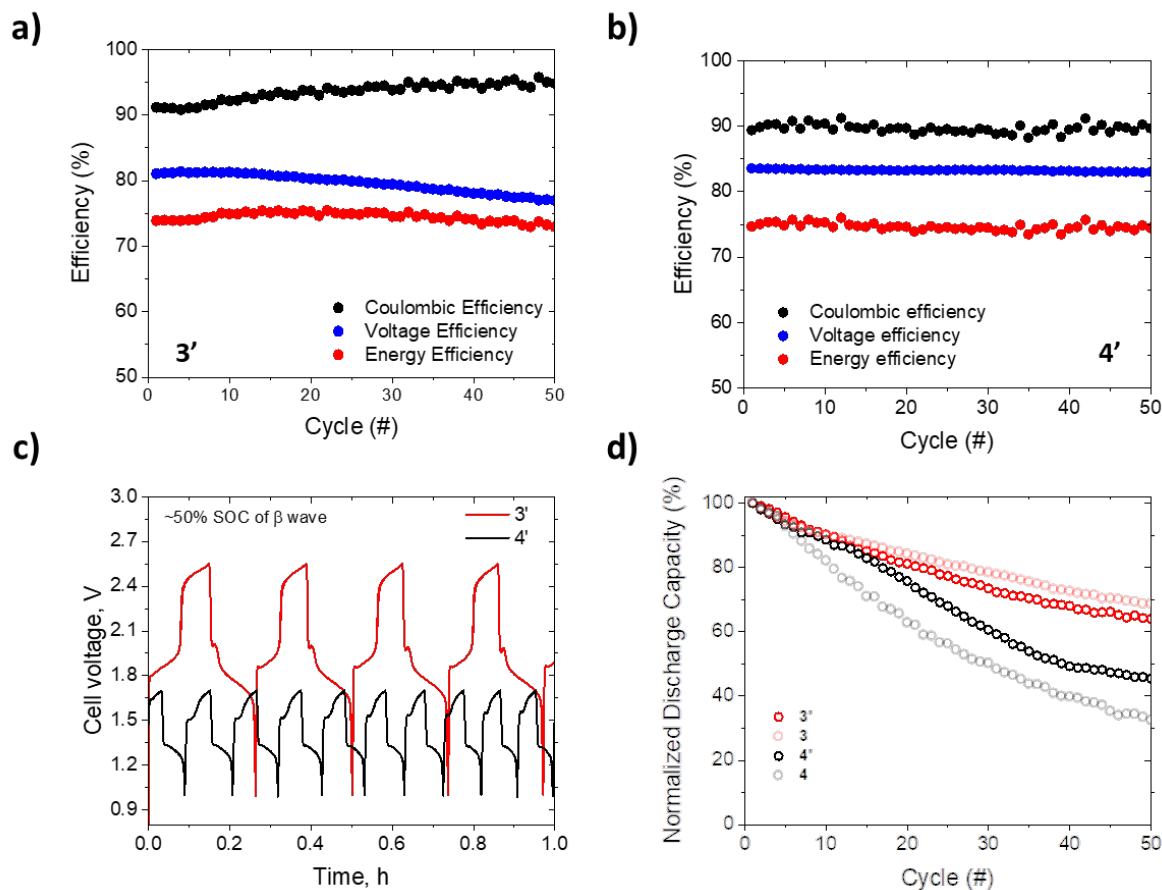
Figure 6. Charge-discharge efficiencies and cycling curves of **3'** and **4'** (plot a, b, c) at 5 mA cm^{-2}, ~50% SOC of β wave. Capacity retention during the charge-discharge cycles (plot d). Conditions: 5 mM of **3'** and **4'**, 10 mM of Fc and 0.25 M of TEABF$_4$ in MeCN.

Theoretical Modeling

Density functional theory (DFT) calculations were performed to explore the impact of incorporating quaternary ammonium cations into the ligand scaffold of **3** and **4** from the electronic structure perspective. We determined the nature of redox events, analyzed composition/energy levels of molecular orbitals (MOs), and assessed structural changes of **3/4** *vs.* **3'/4'** at all respective charge states. The geometrical parameters of the experimentally available complexes are reproduced well in the optimized structures (Tables S8, S9), with the Fe-N and Ni-N bond lengths

20

deviating by less than 2.3% and 1.1% from the XRD data, respectively, providing confidence in the employed level of theory. Analysis of their geometrical structures shows that there are some alterations occurring due to the addition of the quaternary alkyl ammonium moiety, but many features remain qualitatively similar across all charge states (see SI for details). Theoretical analyses of redox properties for the parent complexes, **3** and **4**, have been reported previously,[35,36] and, as such, the same respective level of theory was employed to describe the newly reported counterparts, **3'** and **4'**. All calculations were performed in the absence of outer sphere counterions; hence the following ranges of charge states were considered for the calculations involving **3**, **3'**, **4**, and **4'**: $\{+1 \rightarrow -2\}$, $\{+2 \rightarrow -1\}$, $\{+3 \rightarrow -1\}$, and $\{+4 \rightarrow 0\}$, respectively.

Impact on Redox Potentials and Nature of Redox Events

Most of the calculated redox potentials are found to be within 0.2 V of the corresponding experimental values (Figure 7), in agreement with the expected deviation for calculations involving the revised Born-Haber approximation.[53] This approach has previously been successfully applied to other Fe- and Ni-based charge carriers as described elsewhere.[54,55] In concordance with the experimental values, our calculations show that the introduction of the quaternary alkyl ammonium moiety to **3** and **4** generally makes the redox potentials slightly more positive (Table S10). A few of the computed redox potentials were overestimated, producing appreciably more positive values than those seen experimentally (see SI for a discussion on the dependence of spin-state energetics on the employed DFT functional).
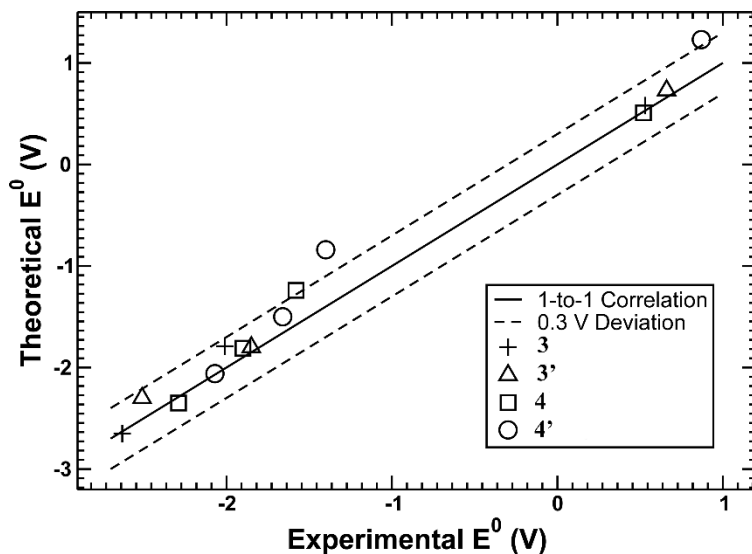
Figure 7. Theoretical *vs.* experimental redox potentials (V) of **3**, **3'**, **4**, and **4'** in the $\{+1 \rightarrow -2\}$, $\{+2 \rightarrow -1\}$, $\{+3 \rightarrow -1\}$, and $\{+4 \rightarrow 0\}$ range of charge states, respectively. 1-to-1 correlation and 0.3 V deviation lines are shown for visualization purposes.

Analysis of the Mulliken spin density shows that the nature of the redox events, whether it is a metal- or ligand-based oxidation/reduction reaction, is not qualitatively affected by the addition of the quaternary alkyl ammonium (Table S10), replicating our previous calculations for **3** and **4**.[35,36] In both Ni complexes, the positive δ wave and first negative wave, χ, occur on the metal, as evidenced by the Mulliken spin density on the Ni center in $\mathbf{3}^{1+/1-}$ (1.12/0.89) and $\mathbf{3'}^{2+/0}$ (1.11/0.89) (Tables S13, S14). The second negative wave, β, occurs on the pyridyl ligand, producing an open-shell singlet in both Ni complexes, where the unpaired electrons on the metal and the pyridyl ligand are configured in an antiferromagnetic fashion, *i.e.,* -0.93/-0.91 on Ni and 0.92/0.87 on pyridyl rings in **3/3'**. In both Fe complexes, the positive δ wave occurs on the metal (Fe^{2+}/Fe^{3+}), but there is a considerable alteration in the magnitude of Mulliken spin density on the metal with the addition of the pendent quaternary ammonium group. Specifically, while there is a competition between the Fe center (0.61) and tripodal NC_6 moiety (0.43) in $\mathbf{4}^{3+}$, the additional positive charge in $\mathbf{4'}^{4+}$ removes the electron density from the ligand, making it a purer $Fe^{2+} \rightarrow Fe^{3+}$ redox event (Tables S15, S16). In the χ, β, and α waves, all three reductions occur primarily on

22

the imino-pyridine ligands, with little deviation in the Mulliken spin density between **4** and **4'**. An increased spin on Fe in the α wave in both complexes (0.57) agrees with the decreased π-acceptor capacity of the imino-pyridine ligands in the most negatively charged states.

Impact on Molecular Orbital Composition and Energy Levels

Comparison of the MO energy levels shows that the highest occupied molecular orbital (HOMO) of **3'/4'** becomes lower in energy upon the addition of the quaternary ammonium moiety, highlighting the effect of the more positive molecular charges of **3'/4'** relative to **3/4** in their respective charge states (Figure 8, S32-S40). The larger effect is seen for the Fe complexes when compared to the Ni complexes (0.32-1.34 eV *vs.* 0.04-0.36 eV), suggesting a greater impact of the quaternary alkyl ammonium for the Fe-based complexes. Substantial stabilization of the HOMO energy levels found in **4'$^{4+/3+}$** relative to that of **4$^{3+/2+}$** suggests a more difficult oxidation, in agreement with the more positive δ wave and the inability of the modified counterpart to cycle oxidatively. On the other side, incorporation of the quaternary ammonium also impacts the lowest unoccupied molecular orbital energy levels making them more negative relative to the parent complexes, by 0.23-0.81 eV in **4'** and 0.08-0.31 eV in **3'**. Qualitatively,[56] this explains the higher capacity of the modified complexes to get reduced in the χ, β, and α waves, producing more positive redox potentials, which agrees with the greater stability of the negative waves of **4'** compared to **4.**
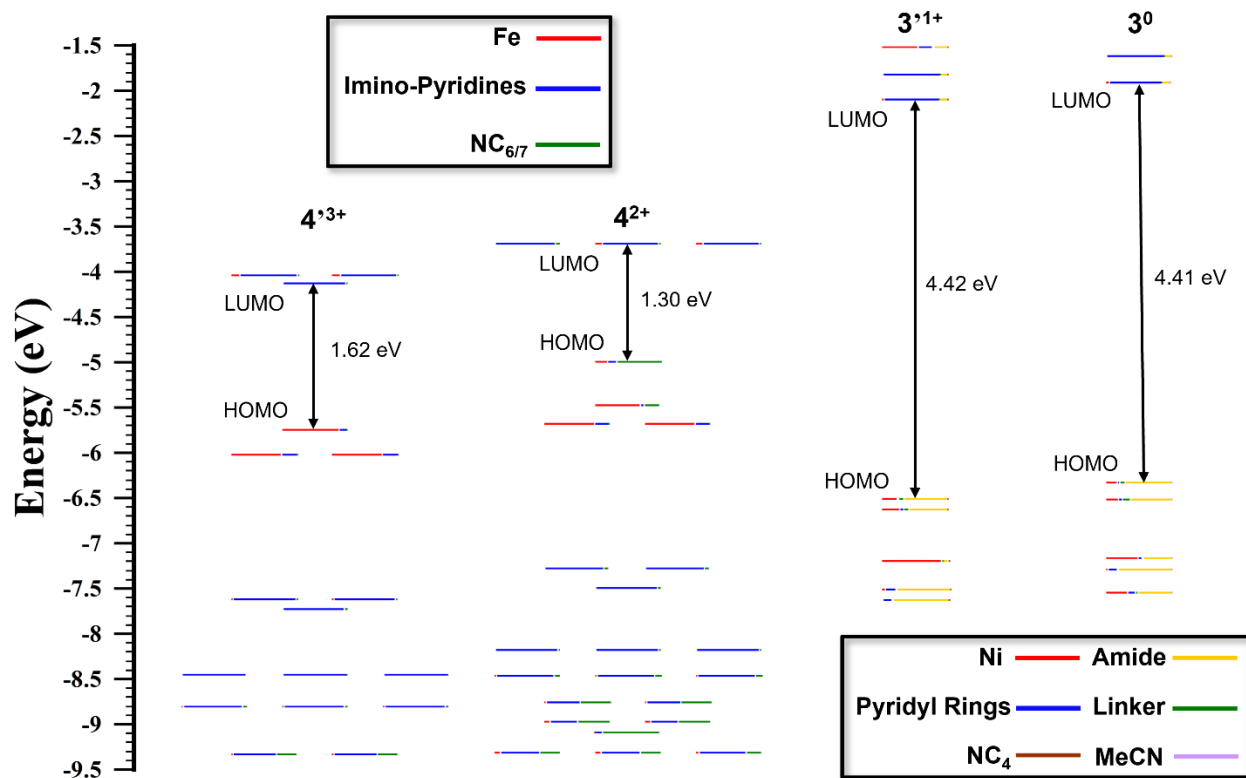
Figure 8. MO composition and energy levels of **4'³⁺** *vs.* **4²⁺** (left), and **3'¹⁺** *vs.* **3⁰** (right). Colors of the MO lines represent the percentage of the AOs of the fragments shown in the black boxes. NC_4 and NC_7 stand for the quaternary alkyl ammonium moieties present in **3'** and **4'**. Linker indicates the alkyl chain connecting picolinamides. Degeneracy of the orbitals is set to 0.05 eV for visualization purposes.

Addition of the quaternary alkyl ammonium group to **3** does not alter the MO compositions significantly, displaying qualitatively similar orbital contributions across all charge states (Figures S32-S35). For both **3'¹⁺** and **3⁰**, the frontier MOs contain substantial contribution from the amide moiety (~65.9% and ~70.3%, respectively), suggesting that the ligands can compete with the metal center for electron removal upon oxidation. This agrees with the appreciable amount of the spin density on the amide in **3'²⁺** (-0.17) and **3¹⁺** (-0.19) as compared to the Ni center in these complexes (1.11 and 1.12, respectively) (Tables S13, S14). Our previous studies of the bispicolinamide Ni complex with a phenyl linker, Ni(bpb), showed that introducing a redox active linker instead of an alkyl chain or adding electron donating/withdrawing groups may alter the nature of the redox events in the negative waves making the metal- and ligand-centered reactions energetically

24

indistinguishable.[17] The first reduction of both Ni complexes populates the α-HOMO orbital with primarily Ni AOs (~45.1% in $\mathbf{3'^0}$ and ~46.4% in $\mathbf{3^{1-}}$) and some amide AOs (~35.2% and ~33.7%, respectively), substantiated by the dominant Mulliken spin densities on Ni in both complexes. In the second reduction, the α-HOMO is predominantly composed of pyridyl AOs, indicating a pyridyl-based reduction.

The MO diagram for $\mathbf{4^{2+}}$ shows a significant contribution from the tripodal NC_6 moiety at the HOMO level (%NC_6 AOs = 68.2%), which is in stark contrast to its counterpart $\mathbf{4'^{3+}}$ displaying an Fe-dominant (%Fe AOs = 86.5%) frontier orbital (Figures 8, S37). While the MO diagrams of both oxidized complexes qualitatively display a metal-based oxidation in the δ wave (Figures S36, S37), the increased portion of the ligand AOs in the HOMO of $\mathbf{4^{2+}}$ offers an opportunity to alter the nature of this event to a ligand-based one by employing functional groups that could facilitate ligand oxidation. The three consecutive reductions describing the negative χ, β, and α waves subsequently populate three frontier α-MOs with pyridyl AOs in both $\mathbf{4}$ and $\mathbf{4'}$ (Figures S38-S40), accounting for the doublet, triplet, and quartet spin state species, respectively.

CONCLUSIONS

In a continuing effort to develop redox flow battery charge carriers with improved cycle performance and reduced cost, we successfully assessed the benefits of incorporating pendent quaternary alkyl ammonium moieties into the ligand of two base-metal (Fe, Ni) complexes. The solubility for $\mathbf{3'}$ improved dramatically by 283%, although in an absolute and practical sense the change from 9 mM to 25 mM does not result in much change for stored energy density.[10] Complex $\mathbf{4'}$, synthesized from an already a positively charged complex, actually exhibited a reduction in solubility (0.31 M) compared to $\mathbf{4}$ (0.54 M), for reasons currently unknown. The incorporation of the ammonium moiety causes a shift in redox features by cyclic voltammetry, with both complexes

exhibiting a small positive shift in their redox waves of ~0.1 V for **3'** and ~0.2 V for **4'**. There is

also notable reduction in reversibility of one wave in each complex, the most negative or β wave

in **3'** and the most positive δ wave in **4'**. Analysis of the Mulliken spin densities and MO energy

diagrams for the complexes confirm that the location of the redox events remains qualitatively the

same in the modified complexes. In **4'**, there is a significant decrease in the participation of the

AOs pertaining to the NC_7 moiety when compared to the analogous contribution of NC_6 in its

unmodified counterpart. The positive charge from the pendent quaternary alkyl ammonium

reduces the competition between the metal and the ligand for the oxidation event and puts more

emphasis on the Fe center, creating a purer metal-based oxidation. Geometrical analysis of the

complexes across the charge states shows similarities between the modified and unmodified

counterparts in most cases, with the largest difference seen in **4'** displaying a proclivity to distance

its charged Fe center from the positively charged NC_7 moiety, as one would expect for similarly

charged species. Although the geometric structures do not show significant alterations between the

parent and the modified complexes across their respective charge states, the electrochemical

performance is quite different. While the CV data for **3'** indicates less reversibility of the β wave

($i_c/i_a = 0.59$ vs. 1.05 for **3**), we were able show some bulk cycling of both χ and β waves in contrast

to complex **3**. Flow experiments appear to reflect the reversibility changes observed in CV

measurements, with the capacity decay of complex **3'** being slightly faster than **3**. Overall, there

is not a distinct benefit to incorporating positively charged groups onto complex **3**. Complex **4'**,

by contrast, exhibited the opposite quality with improved reversibility of the β wave ($i_c/i_a = 1.03$

vs. 0.82 for **4**) in the CV and worse bulk cycling of χ and β whereby utilization was never > 1

electrons/molecule (vs. > 1.8 electrons/molecule with **4**). Complex **4'** as a negolyte in a flow cell

demonstrated excellent cycling with the χ wave (Figure 5) compared to **4**; this improvement was

diminished when cycling the χ wave and ~50% SOC of β. The improved cycling of the β wave in complex **4** came with a cost in the reduced reversibility of its positive wave, indicating this approach can improve negolytic function. Overall, the incorporation of an ammonium cation in the ligand did improve either solubility, cyclability of negative waves, or both in the base-metal complex charge carriers studied, in contrast to previous work on Fc.[25] Future work will concentrate on the elucidation of the degradation pathways and how to inhibit those processes for improved cyclability, since fully reversible waves in complexes **3** and **4** could enable 3V open-circuit voltage.

ASSOCIATED CONTENT

Supporting Information. Additional description of general methods, synthesis, characterization, spectroscopy, solubility, crystallography, electrochemical measurements, and modeling data are detailed in the SI.

AUTHOR INFORMATION

Corresponding Author

*****Benjamin L. Davis, Email: bldavis@lanl.gov; Sandip Maurya, Email: smaurya@lanl.gov; Ivan A. Popov, Email: ipopov@uakron.edu

Author Contributions

The manuscript was written through contributions of all authors. All authors have given approval to the final version of the manuscript.

ACKNOWLEDGMENT

REFERENCES

(1)   Comstock, O. *Today in Energy EIA expects renewables to account for 22 % of U . S . electricity generation in 2022*. August 16. https://www.eia.gov/todayinenergy/detail.php?id=53459.

(2)   Cairns, R. *This giant "water battery" under the Alps could be a game- changer for renewable energy in Europe*. CNN. https://www.cnn.com/2022/08/01/world/water-battery-switzerland-renewable-energy-climate-scn-hnk-spc-intl/index.html.

(3)   Mann, M.; Putsche, V.; Shrager, B. *Grid energy storage supply chain deep dive assessment*. U. S. Department of Energy Response to Executive Order 14017, "America's Supply Chains." https://doi.org/10.2172/1871557.

(4)   Uria-Martinez, R.; Johnson, M.; Rui, S. *U.S Hydropower Market Report - Water power technologies office*. Office of Energy Efficiency & Renewable Energy. https://doi.org/10.2172/1763453.

(5)   Hoffstaedt, J. P.; Truijen, D. P. K.; Fahlbeck, J.; Gans, L. H. A.; Qudaih, M.; Laguna, A. J.; De Kooning, J. D. M.; Stockman, K.; Nilsson, H.; Storli, P. T.; Engel, B.; Marence, M.; Bricker, J. D. Low-Head Pumped Hydro Storage: A Review of Applicable Technologies for Design, Grid Integration, Control and Modelling. *Renewable and Sustainable Energy Reviews* **2022**, *158* (February), 112119. https://doi.org/10.1016/j.rser.2022.112119.

(6)   Vilanova, M. R. N.; Flores, A. T.; Balestieri, J. A. P. Pumped Hydro Storage Plants: A Review. *Journal of the Brazilian Society of Mechanical Sciences and Engineering* **2020**, *42* (8), 1–14. https://doi.org/10.1007/s40430-020-02505-0.

(7)   Ardizzon, G.; Cavazzini, G.; Pavesi, G. A New Generation of Small Hydro and Pumped-Hydro Power Plants: Advances and Future Challenges. *Renewable and Sustainable Energy Reviews* **2014**, *31*, 746–761. https://doi.org/10.1016/j.rser.2013.12.043.

(8)   Shan, R.; Reagan, J.; Castellanos, S.; Kurtz, S.; Kittner, N. Evaluating Emerging Long-Duration Energy Storage Technologies. *Renewable and Sustainable Energy Reviews* **2022**, *159* (February), 112240. https://doi.org/10.1016/j.rser.2022.112240.

(9)   Chen, R.; Bresser, D.; Saraf, M.; Gerlach, P.; Balducci, A.; Kunz, S.; Schröder, D.; Passerini, S.; Chen, J. A Comparative Review of Electrolytes for Organic-Material-Based Energy-Storage Devices Employing Solid Electrodes and Redox Fluids. *ChemSusChem* **2020**, 1–16. https://doi.org/10.1002/cssc.201903382.

(10)   Palmer, T. C.; Beamer, A.; Pitt, T.; Popov, I. A.; Cammack, C. X.; Pratt, H. D.; Anderson, T. M.; Batista, E. R.; Yang, P.; Davis, B. L. A Comparative Review of Metal-Based Charge Carriers in Nonaqueous Flow Batteries. *ChemSusChem* **2021**, *14* (5), 1214–1228. https://doi.org/10.1002/cssc.202002354.

(11)   Soloveichik, G. L. Flow Batteries: Current Status and Trends. *Chemical Reviews* **2015**, *115* (20), 11533–11558. https://doi.org/10.1021/cr500720t.

(12)   Flatt, C.; Sullivan, L. The U.S. Made a Breakthrough Battery Discovery — Then Gave the Technology to China. *National Public Radio*. 2022. https://doi.org/https://www.npr.org/2022/08/03/1114964240/new-battery-technology-china-vanadiumis.

(13)   Yan, Y.; Robinson, S. G.; Sigman, M. S.; Sanford, M. S. Mechanism-Based Design of a High-Potential Catholyte Enables a 3.2 v All-Organic Nonaqueous Redox Flow Battery. *J Am Chem Soc* **2019**, *141* (38), 15301–15306. https://doi.org/10.1021/jacs.9b07345.

(14)   Yan, Y.; Walser-Kuntz, R.; Sanford, M. S. Targeted Optimization of Phenoxazine Redox Center for Nonaqueous Redox Flow Batteries. *ACS Mater Lett* **2022**, *4* (4), 733–739. https://doi.org/10.1021/acsmaterialslett.2c00050.

(15)   Yan, Y.; Zhang, L.; Walser-Kuntz, R.; Vogt, D. B.; Sigman, M. S.; Yu, G.; Sanford, M. S. Benzotriazoles as Low-Potential Anolytes for Non-Aqueous Redox Flow Batteries. *Chemistry of Materials* **2022**, *34* (23), 10594–10605. https://doi.org/10.1021/acs.chemmater.2c02682.

(16)   Etkind, S. I.; Lopez, J.; Zhu, Y. G.; Fang, J. H.; Ong, W. J.; Shao-Horn, Y.; Swager, T. M. Thianthrene-Based Bipolar Redox-Active Molecules Toward Symmetric All-Organic Batteries. *ACS Sustain Chem Eng* **2022**, *10* (36), 11739–11750. https://doi.org/10.1021/acssuschemeng.2c01717.

(17)   Andrade, G. A.; Popov, I. A.; Federico, C. R.; Yang, P.; Batista, E. R.; Mukundan, R.; Davis, B. L. Expanding the Potential of Redox Carriers for Flow Battery Applications. *J Mater Chem A Mater* **2020**, *8* (34), 17808–17816. https://doi.org/10.1039/d0ta04511j.

(18)   Nariyama, H.; Ito, S.; Okada, Y.; Inatomi, Y.; Ichikawa, K.; Masumoto, Y.; Fujimoto, M. High Energy Density 3V-Class Redox Flow Battery Using LiFePO4 and Graphite with Organic Bifunctional Redox Mediators. *Electrochim Acta* **2022**, *409*, 139915. https://doi.org/10.1016/j.electacta.2022.139915.

(19)   Makarova, M. V.; Akkuratov, A. V.; Sideltsev, M. E.; Stevenson, K. J.; Romadina, E. I. Novel Ethylene Glycol Substituted Benzoxadiazole and Benzothiadiazole as Anolytes for Nonaqueous Organic Redox Flow Batteries. *ChemElectroChem* **2022**, *9* (15), 1–7. https://doi.org/10.1002/celc.202200483.

(20)   Stauber, J. M.; Zhang, S.; Gvozdik, N.; Jiang, Y.; Avena, L.; Stevenson, K. J.; Cummins, C. C. Cobalt and Vanadium Trimetaphosphate Polyanions: Synthesis, Characterization, and Electrochemical Evaluation for Non-Aqueous Redox-Flow Battery Applications. *J Am Chem Soc* **2018**, *140* (2), 538–541. https://doi.org/10.1021/jacs.7b08751.

(21)   Cabrera, P. J.; Yang, X.; Suttil, J. A.; Hawthorne, K. L.; Brooner, R. E. M.; Sanford, M. S.; Thompson, L. T. Complexes Containing Redox Noninnocent Ligands for Symmetric, Multielectron Transfer Nonaqueous Redox Flow Batteries. *Journal of Physical Chemistry C* **2015**, *119* (28), 15882–15889. https://doi.org/10.1021/acs.jpcc.5b03582.

(22)   Cabrera, P. J.; Yang, X.; Suttil, J. A.; Brooner, R. E. M.; Thompson, L. T.; Sanford, M. S. Evaluation of Tris-Bipyridine Chromium Complexes for Flow Battery Applications: Impact

of Bipyridine Ligand Structure on Solubility and Electrochemistry. *Inorganic Chemistry* **2015**, *54*, 10214–10223. https://doi.org/10.1021/acs.inorgchem.5b01328.

(23)   Moutet, J.; Mills, D.; Hossain, M. M.; Gianetti, T. L. Increased Performance of an All-Organic Redox Flow Battery Model: Via Nitration of the [4]Helicenium DMQA Ion Electrolyte. *Materials Advances* **2022**, *3* (1), 216–223. https://doi.org/10.1039/d1ma00914a.

(24)   Feng, R.; Xin, Z.; Murugesan, V.; Hollas, A.; Chen, Y.; Shao, Y.; Walter, E.; Wellala, N. P. N.; Yan, L.; Rosso, K. M.; Wang, W. Reversible Ketone Hydrogenation and Dehydrogenation for Aqueous Organic Redox Flow Batteries. *Science* **2021**, *3722*, 836–840. https://doi.org/10.1126/science.abd9795.

(25)   Wei, X.; Cosimbescu, L.; Xu, W.; Hu, J. Z.; Vijayakumar, M.; Feng, J.; Hu, M. Y.; Deng, X.; Xiao, J.; Liu, J.; Sprenkle, V.; Wang, W. Towards High-Performance Nonaqueous Redox Flow Electrolyte via Ionic Modification of Active Species. *Advanced Energy Materials* **2015**, *5* (1), 1–7. https://doi.org/10.1002/aenm.201400678.

(26)   Darling, R. M.; Gallagher, K. G.; Kowalski, J. A.; Ha, S.; Brushett, F. R. Pathways to Low-Cost Electrochemical Energy Storage: A Comparison of Aqueous and Nonaqueous Flow Batteries. *Energy Environ Sci* **2014**, *7* (11), 3459–3477. https://doi.org/10.1039/c4ee02158d.

(27)   Wei, X.; Cosimbescu, L.; Xu, W.; Hu, J. Z.; Vijayakumar, M.; Feng, J.; Hu, M. Y.; Deng, X.; Xiao, J.; Liu, J.; Sprenkle, V.; Wang, W. Towards High-Performance Nonaqueous Redox Flow Electrolyte via Ionic Modification of Active Species. *Adv Energy Mater* **2015**, *5* (1), 1–7. https://doi.org/10.1002/aenm.201400678.

(28)   Zhen, Y.; Zhang, C.; Li, Y. Coupling Tetraalkylammonium and Ethylene Glycol Ether Side Chain To Enable Highly Soluble Anthraquinone-Based Ionic Species for Nonaqueous Redox Flow Battery. *ACS Appl Mater Interfaces* **2022**, *14* (15), 17369–17377. https://doi.org/10.1021/acsami.2c01569.

(29)   Zhen, Y.; Zhang, C.; Yuan, J.; Li, Y. Anthraquinone-Based Electroactive Ionic Species as Stable Multi-Redox Anode Active Materials for High-Performance Nonaqueous Redox Flow Batteries. *J Mater Chem A Mater* **2021**, *9* (38), 22056–22063. https://doi.org/10.1039/d1ta04546f.

(30)   Yan, Y.; Robinson, S. G.; Vaid, T. P.; Sigman, M. S.; Sanford, M. S. Simultaneously Enhancing the Redox Potential and Stability of Multi-Redox Organic Catholytes by Incorporating Cyclopropenium Substituents. *J Am Chem Soc* **2021**, *143* (33), 13450–13459. https://doi.org/10.1021/jacs.1c07237.

(31)   Pham-Truong, T. N.; Wang, Q.; Ghilane, J.; Randriamahazaka, H. Recent Advances in the Development of Organic and Organometallic Redox Shuttles for Lithium-Ion Redox Flow Batteries. *ChemSusChem* **2020**, *13* (9), 2142–2159. https://doi.org/10.1002/cssc.201903379.

(32)   Ahn, S.; Jang, J. H.; Kang, J.; Na, M.; Seo, J.; Singh, V.; Joo, J. M.; Byon, H. R. Systematic Designs of Dicationic Heteroarylpyridiniums as Negolytes for Nonaqueous Redox Flow Batteries. *ACS Energy Lett* **2021**, 3390–3397. https://doi.org/10.1021/acsenergylett.1c01623.

(33)   Lantz, A. W.; Shavalier, S. A.; Schroeder, W.; Rasmussen, P. G. Evaluation of an Aqueous Biphenol- and Anthraquinone-Based Electrolyte Redox Flow Battery. *Applied Energy Materials* **2019**, *2*, 7893–7902. https://doi.org/10.1021/acsaem.9b01381.

(34)   Zhang, B.; Schrage, B. R.; Frkonja-Kuczin, A.; Gaire, S.; Popov, I. A.; Ziegler, C. J.; Boika, A. Zwitterionic Ferrocenes: An Approach for Redox Flow Battery (RFB) Catholytes. *Inorg Chem* **2022**, *61* (21), 8117–8120. https://doi.org/10.1021/acs.inorgchem.2c00722.

(35)   Chu, T.; Popov, I. A.; Andrade, G. A.; Maurya, S.; Yang, P.; Batista, E. R.; Scott, B. L.; Mukundan, R.; Davis, B. L. Linked Picolinamide Nickel Complexes as Redox Carriers for Nonaqueous Flow Batteries. *ChemSusChem* **2019**, *12* (7), 1304–1309. https://doi.org/10.1002/cssc.201802985.

(36)   Sharma, S.; Andrade, G. A.; Maurya, S.; Popov, I. A.; Batista, E. R.; Davis, B. L.; Mukundan, R.; Smythe, N. C.; Tondreau, A. M.; Yang, P.; Gordon, J. C. Iron-Iminopyridine Complexes as Charge Carriers for Non-Aqueous Redox Flow Battery Applications. *Energy Storage Materials* **2021**, *37* (October 2020), 576–586. https://doi.org/10.1016/j.ensm.2021.01.035.

(37)   Makarova, M. V.; Akkuratov, A. V.; Sideltsev, M. E.; Stevenson, K. J.; Romadina, E. I. Novel Ethylene Glycol Substituted Benzoxadiazole and Benzothiadiazole as Anolytes for Nonaqueous Organic Redox Flow Batteries. *ChemElectroChem* **2022**, *9* (15), 1–7. https://doi.org/10.1002/celc.202200483.

(38)   Romadina, E. I.; Volodin, I. A.; Stevenson, K. J.; Troshin, P. A. New Highly Soluble Triarylamine-Based Materials as Promising Catholytes for Redox Flow Batteries. *Journal of Materials Chemistry A* **2021**, *9* (13), 8303–8307. https://doi.org/10.1039/d0ta11860e.

(39)   Cruz, H.; Jordão, N.; Amorim, P.; Dionísio, M.; Branco, L. C. Deep Eutectic Solvents as Suitable Electrolytes for Electrochromic Devices. *ACS Sustainable Chemistry and Engineering* **2018**, *6* (2), 2240–2249. https://doi.org/10.1021/acssuschemeng.7b03684.

(40)   Romadina, E. I.; Komarov, D. S.; Stevenson, K. J.; Troshin, P. A. New Phenazine Based Anolyte Material for High Voltage Organic Redox Flow Batteries. *Chemical Communications* **2021**, *57* (24), 2986–2989. https://doi.org/10.1039/d0cc07951k.

(41)   Noack, J.; Roznyatovskaya, N.; Herr, T.; Fischer, P. The Chemistry of Redox-Flow Batteries. *Angewandte Chemie - International Edition* **2015**, *54* (34), 9776–9809. https://doi.org/10.1002/anie.201410823.

(42)   Wang, W.; Xu, W.; Cosimbescu, L.; Choi, D.; Li, L.; Yang, Z. Anthraquinone with Tailored Structure for a Nonaqueous Metal-Organic Redox Flow Batter. *Chemical Communications* **2012**, *48* (53), 6669–6671. https://doi.org/10.1039/c2cc32466k.

(43) DeVos, N.; Maton, C.; Stevens, C. V. Electrochemical Stability of Ionic Liquids: General Influences and Degradation Mechanisms. *ChemElectroChem* **2014**, *1* (8), 1258–1270. https://doi.org/10.1002/celc.201402086.

(44) Hapiot, P.; Lagrost, C. Electrochemical Reactivity in Room-Temperature Ionic Liquids. *Chemical Reviews* **2008**, *108* (7), 2238–2264. https://doi.org/10.1021/cr0680686.

(45) Xue, Z.; Qin, L.; Jiang, J.; Mu, T.; Gao, G. Thermal, Electrochemical and Radiolytic Stabilities of Ionic Liquids. *Physical Chemistry Chemical Physics* **2018**, *20* (13), 8382–8402. https://doi.org/10.1039/c7cp07483b.

(46) Lane, G. H. Electrochemical Reduction Mechanisms and Stabilities of Some Cation Types Used in Ionic Liquids and Other Organic Salts. *Electrochimica Acta* **2012**, *83*, 513–528. https://doi.org/10.1016/j.electacta.2012.08.046.

(47) Chu, T.; Popov, I. A.; Andrade, G. A.; Maurya, S.; Yang, P.; Batista, E. R.; Scott, B. L.; Mukundan, R.; Davis, B. L. Linked Picolinamide Nickel Complexes as Redox Carriers for Nonaqueous Flow Batteries. *ChemSusChem* **2019**, *12* (7), 1304–1309. https://doi.org/10.1002/cssc.201802985.

(48) Sharma, S.; Andrade, G. A.; Maurya, S.; Popov, I. A.; Batista, E. R.; Davis, B. L.; Mukundan, R.; Smythe, N. C.; Tondreau, A. M.; Yang, P.; Gordon, J. C. Iron-Iminopyridine Complexes as Charge Carriers for Non-Aqueous Redox Flow Battery Applications. *Energy Storage Mater* **2021**, *37* (October 2020), 576–586. https://doi.org/10.1016/j.ensm.2021.01.035.

(49) Shinkle, A. A.; Pomaville, T. J.; Sleightholme, A. E. S.; Thompson, L. T.; Monroe, C. W. Solvents and Supporting Electrolytes for Vanadium Acetylacetonate Flow Batteries. *Journal of Power Sources* **2014**, *248*, 1299–1305. https://doi.org/10.1016/j.jpowsour.2013.10.034.

(50) Daub, N.; Janssen, R. A. J.; Hendriks, K. H. Imide-Based Multielectron Anolytes as High-Performance Materials in Nonaqueous Redox Flow Batteries. *ACS Appl Energy Mater* **2021**, *4* (9), 9248–9257. https://doi.org/10.1021/acsaem.1c01490.

(51) Popov, I. A.; Mehio, N.; Chu, T.; Davis, B. L.; Mukundan, R.; Yang, P.; Batista, E. R. Impact of Ligand Substitutions on Multielectron Redox Properties of Fe Complexes Supported by Nitrogenous Chelates. *ACS Omega* **2018**, *3* (11), 14766–14778. https://doi.org/10.1021/acsomega.8b01921.

(52) Sevov, C. S.; Fisher, S. L.; Thompson, L. T.; Sanford, M. S. Mechanism-Based Development of a Low-Potential, Soluble, and Cyclable Multielectron Anolyte for Nonaqueous Redox Flow Batteries. *Journal of the American Chemical Society* **2016**, *138*, 15378–15384. https://doi.org/10.1021/jacs.6b07638.

(53) Roy, L. E.; Jakubikova, E.; Graham Guthrie, M.; Batista, E. R. Calculation of One-Electron Redox Potentials Revisited. Is It Possible to Calculate Accurate Potentials with Density Functional Methods? *Journal of Physical Chemistry A* **2009**, *113* (24), 6745–6750. https://doi.org/10.1021/jp811388w.

(54) Popov, I. A.; Mehio, N.; Chu, T.; Davis, B. L.; Mukundan, R.; Yang, P.; Batista, E. R. Impact of Ligand Substitutions on Multielectron Redox Properties of Fe Complexes Supported by Nitrogenous Chelates. *ACS Omega* **2018**, *3* (11), 14766–14778. https://doi.org/10.1021/acsomega.8b01921.

(55) Popov, I. A.; Davis, B. L.; Mukundan, R.; Batista, E. R.; Yang, P. Catalyst-Inspired Charge Carriers for High Energy Density Redox Flow Batteries. *Frontiers in Physics* **2019**, *6* (JAN), 1–10. https://doi.org/10.3389/fphy.2018.00141.

(56) Koopmans, T. Über Die Zuordnung von Wellenfunktionen Und Eigenwerten Zu Den Einzelnen Elektronen Eines Atoms. *Physica* **1934**, *1* (1), 104–113.

TOC Figure
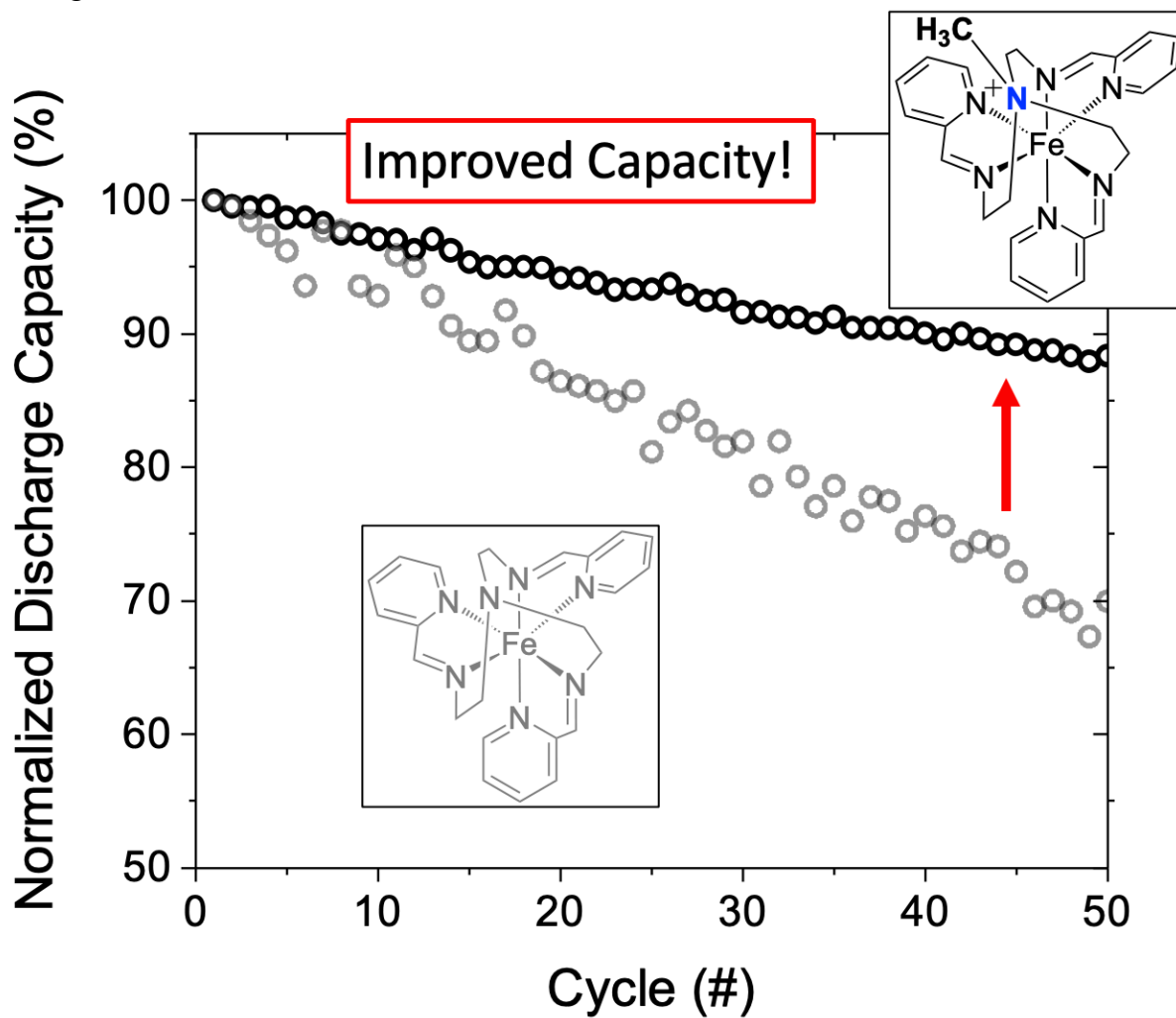
Synopsis: The incorporation of charged ammonium groups in the ligand backbone of nickel and iron complexes can impart improved discharge capacity in redox flow cells.